HyperCEST Detection of a ^{129}Xe-Based Contrast Agent Composed of Cryptophane-A Molecular Cages on a Bacteriophage Scaffold

Todd K. Stevens,[1,2]* Krishnan K. Palaniappan,[1,2] R. Matthew Ramirez,[1,2] Matthew B. Francis,[1,2] David E. Wemmer,[1,3] and Alex Pines[1,2]

A hyperpolarized ^{129}Xe contrast agent composed of many cryptophane-A molecular cages assembled on an M13 bacteriophage has been demonstrated. Saturation of xenon bound in the large number of cryptophane cages is transferred to the pool of aqueous-solvated xenon via chemical exchange, resulting in efficient generation of hyperCEST contrast. No significant loss of contrast per cryptophane cage was observed for the multivalent phage when compared with unscaffolded cryptophane. Detection of this phage-based hyperCEST agent is reported at concentrations as low as 230 fM, representing the current lower limit for NMR/MRI-based contrast agents. **Magn Reson Med 69:1245–1252, 2013.** © **2012 Wiley Periodicals, Inc.**

Key words: xenon; M13 bacteriophage; hyperCEST; cryptophane

INTRODUCTION

Molecular imaging aims to detect the presence and map the spatial distribution of tissue biomarkers that are of specific interest in biological systems under investigation. For many diseases such as cancer, early detection of the important biomarkers when they exist at very low concentrations maximizes the diagnostic and prognostic value. Because of MRI's inherent lack of signal sensitivity, it is difficult to generate contrast between normal and diseased tissue at these early disease stages with conventional imaging. Consequently, exogenous contrast agents are often used to generate unique contrast since many agents can be detected at lower concentrations than endogenous spins. The most common agents, principally gadolinium chelates (1), enhance water relaxation through paramagnetic interactions. Other types of agents that are being developed include paramagnetic shift reagents (e.g., anisotropic lanthanide chelates) enabling chemical exchange saturation transfer (CEST) contrast (2), super-paramagnetic iron oxide field perturbation agents (3), and agents incorporating or composed of non-proton spin nuclei—both thermally polarized (^{19}F) (4) and hyperpolarized (^{13}C, ^{3}He, ^{129}Xe, ^{15}N, ^{19}F) (5–9). However, these MRI agents lack the sensitivity of positron emission tomography and single-photon emission computed tomography nuclear medicine techniques in which the radioactive tracers can be detected at sub-nanomolar concentrations (10); these lower detection thresholds better reflect the desired detection sensitivity for clinically relevant targeted molecular imaging applications.

Recently developed MRI contrast agents called xenon biosensors (11) have demonstrated the ability to utilize the complementary sensitivity enhancements of both hyperpolarized ^{129}Xe and CEST detection (12). The resulting "hyperCEST" contrast mechanism has demonstrated detection thresholds of these biosensors that are several orders of magnitude lower than those of the previously mentioned MRI agents—down to 10 nM (13). Xenon biosensors use cryptophane-A molecular cages (CryA) (14) to reversibly bind xenon atoms that have been dissolved into environments such as aqueous tissue. These constructs can also be functionalized with application specific targeting moieties (11,12,15–21). The CryA bound xenon atoms (Xe@CryA) are in continuous exchange with the more abundant pool of solvated xenon nuclei that are diffusing in the surrounding aqueous environment (Xe@water). Because of the highly sensitive chemical shift response of ^{129}Xe to its local environment, two distinct resonance frequencies representing the Xe@CryA and Xe@water pools can be individually detected and manipulated at chemical shifts of approximately 60 ppm and 190 ppm downfield from the ^{129}Xe gas frequency, respectively. By applying saturating radiofrequency pulses at the ^{129}Xe@CryA frequency for a period that is long compared to the mean xenon residence time inside CryA (the inverse of the dissociation rate), the CEST mechanism allows a single biosensor molecule to saturate the magnetization of hundreds of ^{129}Xe@water nuclei. The complementarity of hyperpolarization and CEST arises from the fact that the bulk spin pool is typically made up of a low concentration of highly polarized ^{129}Xe spins (xenon dissolves to approximately 3 mM in aqueous solutions at 1 atm and 310 K,[1] resulting in 0.8 mM of the ^{129}Xe isotope) as opposed to a high concentration of weakly polarized spins (typically 40 M H_2O

[1]Materials Sciences Division, Lawrence Berkeley National Laboratory, Berkeley, California, USA.

[2]Department of Chemistry, University of California, Berkeley, California, USA.

[3]Physical Biosciences Division, Lawrence Berkeley National Laboratory, Berkeley, California, USA.

Grant sponsor: NSERC (Postdoctoral Fellowship award to T.K.S.); Grant sponsor: U.S. Department of Energy; Grant number: DE-AC02-05CH11231; Grant sponsor: U.S. Department of Defense Breast Cancer Research Program; Grant number: BC061995.

*Correspondence to: Todd K. Stevens, Ph.D., QB3 Stanley Hall, Room 208C, University of California, Berkeley, CA 94720. E-mail: tkstevens@gmail.com

Received 23 February 2012; revised 17 May 2012; accepted 18 May 2012.

DOI 10.1002/mrm.24371

Published online 12 July 2012 in Wiley Online Library (wileyonlinelibrary.com).

[1]Calculated from an Ostwald solubility coefficient of 0.0797 (22).

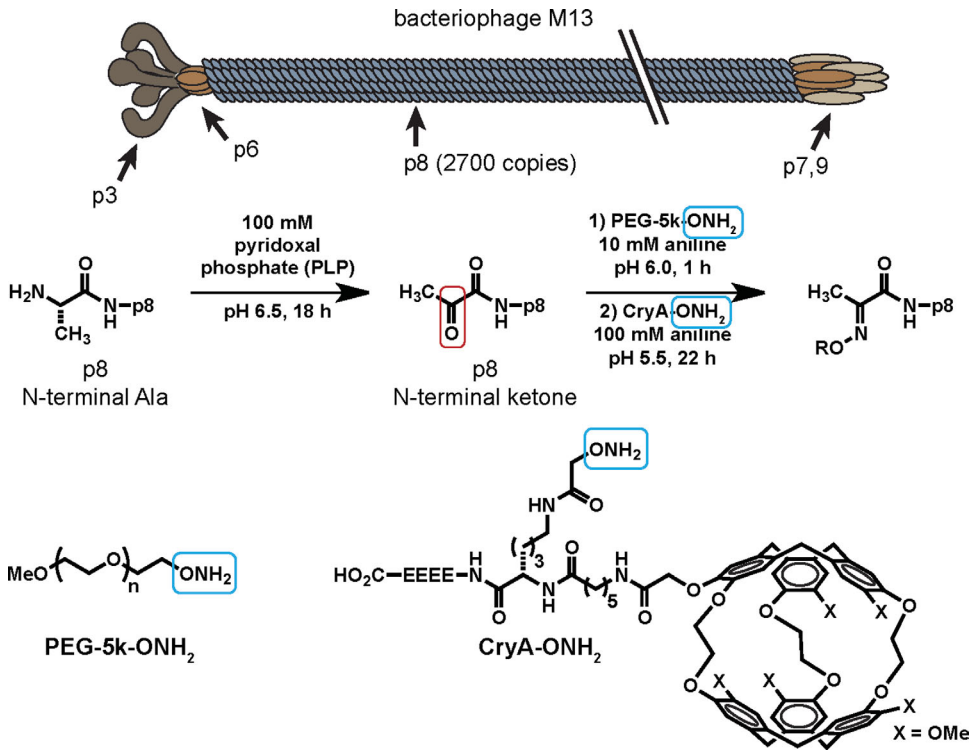

FIG. 1. A cartoon (above) and chemical scheme (below) illustrating the transamination and the attachment of synthetic molecules to bacteriophage M13 (significant proteins are labeled with arrows). The N-termini of the p8 proteins (blue ovals) are transaminated to yield thousands of ketones along the length of the capsids. The ketones are then reacted with PEG-5k—ONH_2 polymer chains, followed by reaction with aminooxy-functionalized cryptophane-A cages (CryA—ONH_2), to construct the M13-based biosensor. The double slash indicates that the phage is much longer than shown when scaled to the minor coat proteins. [Color figure can be viewed in the online issue, which is available at wileyonlinelibrary.com.]

or higher in tissue) for ^{1}H-based CEST. Consequently, each xenon biosensor only has to saturate a modest number of ^{129}Xe@water spins to elicit significant contrast. Furthermore, the hyperCEST detection scheme can be used quickly relative to the long T_1 relaxation times of ^{129}Xe [approximately 6–10 s in oxygenated blood at 1.5 T (23,24) and 60 s in aqueous solvents at 4.7 T (25)] to minimize relaxation-based contrast loss. To improve the detection sensitivity of biologically targeted agents further, multiple copies of CryA have been assembled onto supramolecular scaffolds, such as branched dendrimers (26) and viral capsids (27), which can then be further functionalized with targeting groups. This scaffolding approach has also been explored for PARACEST agents (28).

In this work, the filamentous bacteriophage M13 was selected as an advantageous scaffold for molecular imaging development based on two principal criteria. First, filamentous phage such as the M13 and fd types are routinely used in phage display techniques for identifying new epitope targeting groups such as antibody fragments (29,30). Consequently, established phage display techniques can produce M13 phage that have high binding affinities for application-specific targets such as biomarkers of disease. Second, the single-stranded DNA of the M13 bacteriophage is coated with approximately 2700 identical copies of its major coat protein (p8), on which a large number of CryA cages can be covalently attached using site-specific protein bioconjugation techniques (31–33). The result is an increase in CryA payload per targeted biomarker that is bound by the modified phage. Additionally, phage modification also presents an opportunity to decorate the CryA-bearing scaffold with polyethylene glycol (PEG), which can aid in the solubility and biocompatibility of the agent. The extent to which the hyperCEST-based contrast scales with the number of CryA cages per agent is dependent on several parameters, including changes in the xenon exchange dynamics and bound ^{129}Xe linewidths (due to slower molecular tumbling of the macromolecular scaffold), and thus must be investigated.

The purposes of this study were to investigate the feasibility of using M13 bacteriophage modified with CryA molecular cages as a hyperpolarized xenon MR contrast agent, to compare the hyperCEST response of this phage-based agent relative to unscaffolded CryA, and to establish an in vitro concentration threshold for detecting CryA-modified M13.

METHODS

Agent Preparation

To generate the CryA-modified M13, the protein capsid of the bacteriophage was site-selectively modified. Of the

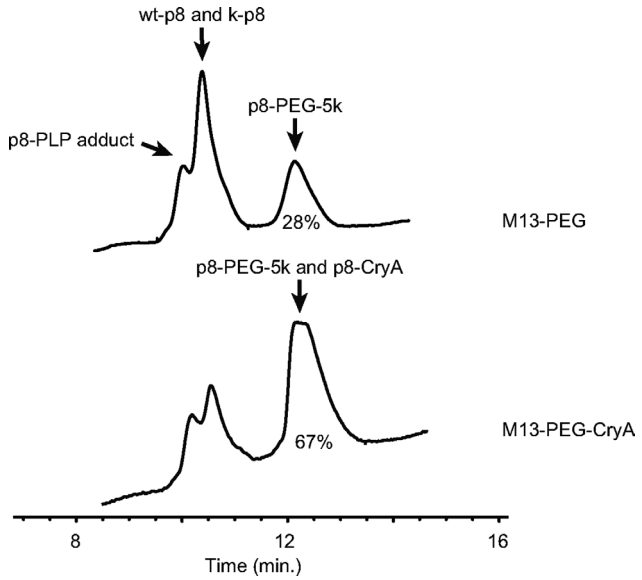

FIG. 2. Characterization of modified phage by RP-HPLC. On average, the p8 coat proteins of the M13-based biosensor were approximately 28% modified with PEG-5k (760 copies, top trace) and approximately 39% modified with CryA (1050 copies, bottom trace). Unbound CryA—ONH_2 elutes in the void volume under these chromatographic conditions, and was not seen in the M13-PEG-CryA sample after gel-filtration purification.

five coat proteins that surround the genetic material of M13 phage (illustrated in Fig. 1), the p8 protein is the most abundant with approximately 2700 copies. To functionalize the p8 protein, the M13 underwent a pyridoxal 5′-phosphate mediated biomimetic transamination reaction (65 nM M13 and 100 mM pyridoxal 5′-phosphate in 150 mM phosphate buffer, pH 6.3, for 18 h at 298 K) (34) to introduce ketone groups at the N-termini of these proteins (termed k-p8, Fig. 1). Further details of this reaction and characterization of the resulting phage have been reported elsewhere (unpublished data). This product (k-M13) was purified through a series of precipitations and resuspensions in Dulbecco's phosphate-buffered saline. To improve solubility and bioavailability of the construct, some of the ketone groups were reacted with aminooxy-functionalized 5 kDa PEG (PEG-5k—ONH_2) (35) (20 nM k-M13 and 20 mM PEG-5k—ONH_2 with 10 mM aniline in 150 mM phosphate buffer, pH 6.0, for 1 h at 293 K). Following gel filtration purification (illustra NAP-5 column, GE Healthcare), the PEG-modified M13 (M13-PEG) was reacted with an aminooxy-functionalized CryA-peptide (CryA—ONH_2) (13 nM M13-PEG and 240 μM aminooxy CryA with 100 mM aniline in 150 mM phosphate buffer, pH 5.5, for 22 h at 293 K), modifying some of the remaining N-terminal ketone groups (Fig. 1). The resulting M13-PEG-CryA conjugate, henceforth termed M13-based biosensor, was purified by gel filtration. Characterization and quantification of the intermediates and final products were performed using a combination of spectrophotometry (Nanodrop 2000, Thermo Fisher Scientific, MA), reverse phase-high performance liquid chromatography (RP-HPLC, 1100 Series, Agilent Technologies, CA) and electrospray ionization mass spectrometry (LTQ Orbitrap XL, Thermo Fisher Scientific). On average, the p8 coat proteins of the M13-based biosensor were approximately 28% modified with PEG-5k (760 copies) and approximately 39% modified with CryA (1050 copies) (Fig. 2). While PEG-5k was required to ensure the aqueous solubility of the phage following the high level of modification with hydrophobic CryA, the level of PEG-5k modification was controlled to allow sufficient access to the ketone groups for the subsequent CryA attachment. Moreover, the CryA modification was controlled to balance the desire for high CryA payloads with the need for maintaining aqueous solubility. The construct was dissolved in filtered Dulbecco's phosphate-buffered saline (pH 7.4) for ^{129}Xe NMR testing. Control NMR experiments were performed with solutions containing unscaffolded CryA-peptide (i.e., CryA—ONH_2) in Dulbecco's phosphate-buffered saline. Further details on the CryA—ONH_2 synthesis and phage characterization are provided as an appendix.

NMR Experiments

A pressurized xenon gas mixture (2% natural abundance xenon, 10% nitrogen, and 88% helium at 584 kPa) was hyperpolarized to approximately 5% with a MITI Xeno-Spin spin exchange optical pumping polarizer (GE Healthcare, formerly Nycomed Amersham, Buckinghamshire, UK) and dissolved into 650 μL of biosensor solution by bubbling through a small capillary into a 5 mm NMR tube modified with a gas outflow elbow (Fig. 3). For every sample tested, a small amount (0.002% v/v) of a low hydrophilic–lipophilic balance surfactant (Pluronic F-68, BASF, Edison, NJ) was added to minimize foaming as well as potential stress on any proteins in solution during bubbling. Before each pulse sequence repetition, the xenon mixture was bubbled at a flow rate of approximately 0.05 SLM to saturate the solution with hyperpolarized ^{129}Xe, followed by a wait period to allow the solution to settle and bubbles to clear. The gas transit

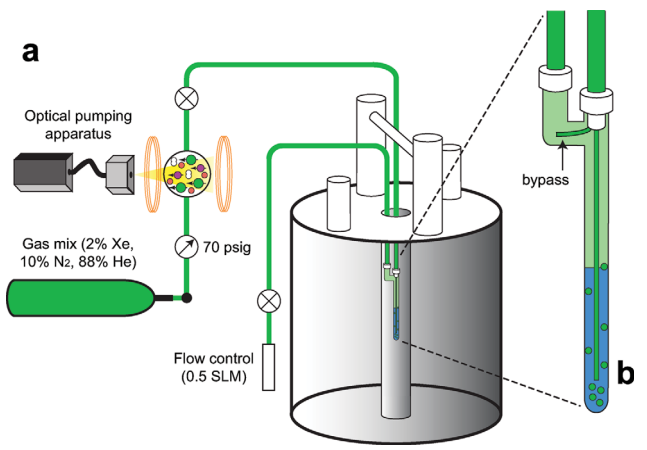

FIG. 3. Schematic of the NMR experimental setup. Shown in (a) is a simplified flow path of the xenon gas mixture, including polarization via a spin exchange optical pumping polarizer, introduction of the gas into the biosensor solution via bubbling through a small capillary, and valves for pausing gas flow during NMR acquisitions. A zoomed in view of the specialized glassware and bubbling setup is shown in (b). [Color figure can be viewed in the online issue, which is available at wileyonlinelibrary.com.]

Table 1
The Relevant Frequency Offsets Used for CEST Experimentation (Referenced to the ^{129}Xe Gas Frequency)

Temperature	^{129}Xe@water	^{129}Xe@CryA (unscaffolded)	^{129}Xe@CryA (M13-based)
293 K	192.0 ppm	59.4 ppm (on)	61.8 ppm (on)
		324.6 ppm (off)	322.2 ppm (off)
310 K	192.4 ppm	62.2 ppm (on)	64.6 ppm (on)
		322.6 ppm (off)	320.2 ppm (off)

"On" and "off" refer to the on-resonance and control off-resonance frequencies at which RF saturation was applied.

time from the polarizer was minimized by diverting approximately 90% of the higher (0.5 SLM) gas flow through the polarizer to a bypass just before the capillary input. For the CEST spectra and temperature dependence data in which concentrated biosensor samples were used (described below), the solutions were bubbled for 25 s with a wait period of 2 s. To reduce the shot noise for the low concentration biosensor samples used in the dilution series experiments (described below), bubbling and wait times of 40 s and 10 s, respectively, were used.

NMR experiments were performed on a 7.05 T Varian ^{UNITY}INOVA vertical bore spectrometer equipped with a 26-channel shim set and a dual-tuned (^{1}H/^{129}Xe) radiofrequency (RF) saddle coil (i.d. = 5 mm), and all data were collected with a 25 kHz spectral width and an acquisition time of 0.5 s. Saturation in the CEST pulse sequences was applied with trains of band selective d-SNOB pulses (36) without interpulse delays, which have been previously demonstrated to have high saturation efficiency in xenon biosensor systems (37). All data were line broadened with an 8 Hz Lorentzian and fitted in the time domain using a nonlinear least-squares regression (MATLAB; MathWorks, Natick, MA), producing signal amplitudes for subsequent analyses.

To compare the Xe@CryA response for the M13-based biosensor relative to the unscaffolded CryA control, CEST spectra were acquired for a 2.3 nM solution of M13-based biosensor and an unscaffolded solution containing an approximately equivalent amount of CryA (2.2 μM) at 293 K. Saturation was applied with a 10 s train of 500 Hz bandwidth d-SNOB pulses (5.64 ms, 59 μT peak field strength; specific absorption rate (SAR) equivalent B_1 of a 35 μT continuous wave pulse) over a frequency offset range of −32 to 390 ppm. Randomized saturation frequency order allowed for retrospective baseline corrections due to slow temporal variations in the hyperpolarized ^{129}Xe signals were required. Furthermore, the CEST dynamics for these two samples were compared by evaluating contrast versus saturation time at both 293 and 310 K. For these experiments, saturations were applied "on-resonance" at the Xe@CryA frequency and "off-resonance" at an equal distance from the Xe@water frequency but on the downfield side. The offset frequencies were found to vary modestly due to the association with M13 (^{129}Xe@CryA) as well as with temperature (^{129}Xe@CryA and ^{129}Xe@water) (see Results section), and the exact frequencies used in these experiments are presented in Table 1. Saturation durations of up to 20 s were applied using trains of 3 kHz bandwidth d-SNOB pulses (940 μs, 352 μT peak field; SAR equivalent B_1 of a 207 μT continuous wave pulse). Given the differences in saturation times, a variable post-acquisition delay was used to maintain a constant repetition time. Furthermore, it should be noted that undesirable T_1 weightings were already absent from the experiment due to the use refreshed hyperpolarized signals. Plots of the normalized residual signal, equal to (1 − hyperCEST contrast) and expressed as $M_{z,on}/M_{z,off}$, were generated to illustrate the magnitude of the hyperCEST effect alone.

To investigate the dependence of CEST contrast on the concentration of the M13-based biosensor and to determine a detection threshold, plots of residual signal versus saturation time were generated for a dilution series of the biosensor (2.3 nM, 230 pM, 23 pM, 2.3 pM) at 310 K. The NMR acquisition parameters were identical to those described above for the temperature experiments. Finally, a 230 fM M13-based biosensor solution was evaluated as the lower limit concentration using a single saturation duration of 20 s, and the on-resonance and off-resonance data were analyzed with groupwise and paired (one-tailed) Student's *t*-tests.

Preliminary experiments using unmodified M13 were used to confirm the absence of exchangeable signals in the ^{129}Xe CEST spectrum due to the phage itself. Additionally, experiments in solvent alone were used to confirm the absence of baseline asymmetries in the ^{129}Xe@water signal due to the application of 500 Hz and 3 kHz bandwidth d-SNOB pulse trains (peak B_1 and train durations matched to those used in the respective agent experiments) at the on-resonance and off-resonance frequencies (e.g., >10 kHz from the Xe@water frequency).

RESULTS

The full CEST spectra showed Xe@water signal loss arising from saturation at the ^{129}Xe@CryA frequency for both the M13-based biosensor and the unscaffolded CryA

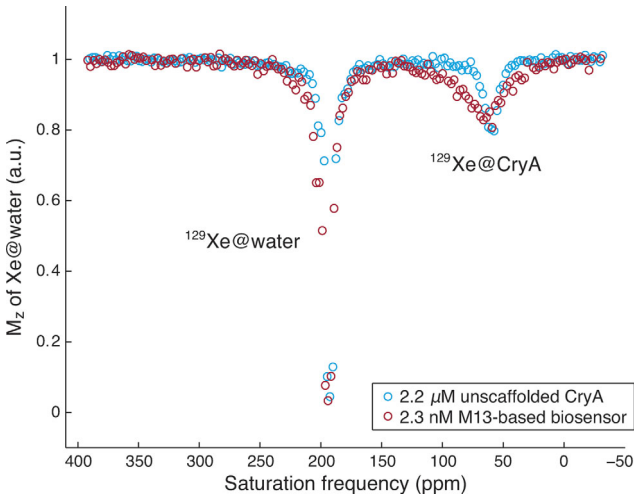

FIG. 4. Comparison of hyperCEST spectra for 2.3 nM M13-based biosensor and a CryA-concentration matched sample of unscaffolded CryA (2.2 μM) acquired at 293 K. Shown are the saturation peaks corresponding to the ^{129}Xe@CryA frequency at approximately 60 ppm and the ^{129}Xe@water frequency at 192 ppm (referenced to the ^{129}Xe gas frequency). [Color figure can be viewed in the online issue, which is available at wileyonlinelibrary.com.]

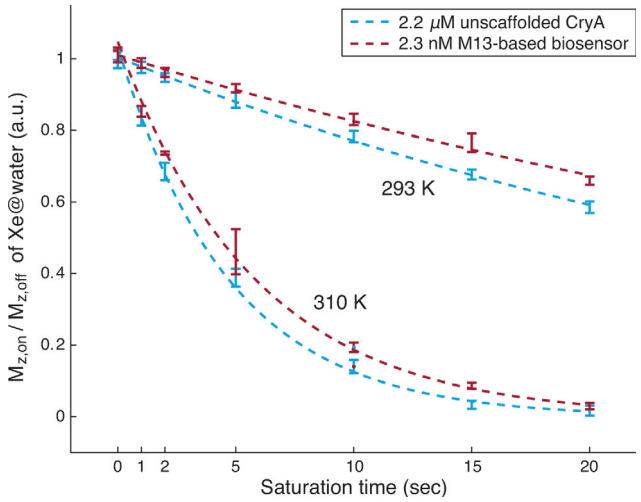

FIG. 5. Plots comparing the loss of Xe@water signal versus saturation time for 2.3 nM M13-based biosensor and 2.2 μM unscaffolded CryA samples. Saturation was applied with a train of 500 Hz bandwidth d-SNOB pulses, and the residual signal, equal to (1 − hyperCEST contrast), is expressed as $M_{z,on}/M_{z,off}$. The error bars represent the mean ± the standard deviation ($n = 4$). The dashed lines represent exponential decay fits of the signal loss.

samples (Fig. 4). Despite a 2.4 ppm downfield shift and broadness in the ^{129}Xe@CryA response of the M13-based biosensor compared to that of the unscaffolded CryA (full width at half minimum of 37.6 ppm versus 13.2 ppm; this observation was expected due to the slower tumbling of the supramolecular phage structure), the maximum contrast for two curves was in good agreement (17% and 19%, respectively). Similarly, the saturation time curves at both 293 and 310 K showed comparable contrast for the M13-based biosensor and the unscaffolded CryA (Fig. 5). As expected, contrast was generated more rapidly at the elevated temperature due to the faster chemical exchange dynamics (e.g., residual signal after 5 s of saturation was 90% and 42% for 293 K and 310 K, respectively). The chemical shifts of ^{129}Xe@CryA and ^{129}Xe@water where shifted downfield 2.8 ppm and 0.4 ppm, respectively, when heating the samples from 293 to 310 K.

For all four concentrations of M13-based biosensor used in the dilution series, CEST contrast was clearly visible in the saturation time curves (Fig. 6), and the decrease in residual signal for each concentration was accurately represented by an exponential decay with saturation time. For these very dilute solutions, the CEST contrast for a given saturation time decreased roughly logarithmically with decreasing M13-based biosensor concentration (Fig. 6, inset).

Impressively, when a 230 fM M13-based biosensor solution was evaluated, statistically significant contrast was demonstrated. Despite the presence of an outlying on-resonance data point (greater than 3 standard deviations from the group mean; Fig. 7, right side of dashed line) for the 230 fM M13-based biosensor sample, a mean contrast of 3.7% was measured ($P < 0.01$ for groupwise and paired t-tests). Excluding the outlying point resulted in a mean contrast of 4.8%.

DISCUSSION AND CONCLUSIONS

This work shows that the filamentous bacteriophage M13 is an effective supramolecular scaffold for multivalent CryA assembly, resulting in a ^{129}Xe-based contrast agent capable of being detected at concentrations as low as 230 fM. This detection threshold represents the best per-agent sensitivity demonstrated for an NMR or MRI contrast agent. CryA produces similar levels of CEST contrast whether in M13-scaffolded or unscaffolded forms, which helps to maximize the increased per-agent sensitivity of the M13 agent being used in this multivalent approach.

The improved per-CryA sensitivity in this study (230 fM M13-based biosensor loaded with 1050 CryA copies per M13 yields 242 pM CryA in solution) relative to

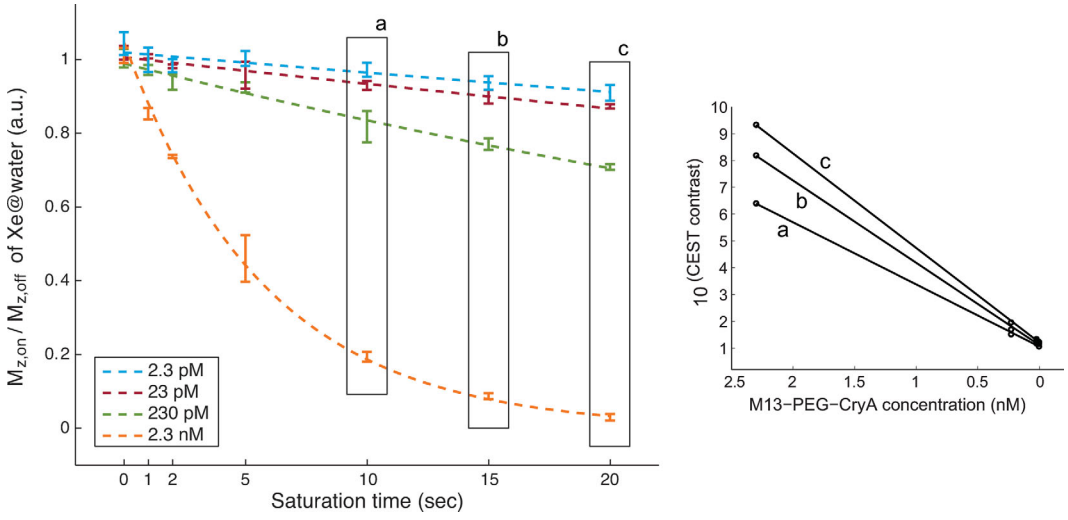

FIG. 6. Plots demonstrating hyperCEST-based Xe@water signal loss versus saturation time for a dilution series of M13-based biosensor samples at 310 K. Saturation was applied with a train of 3 kHz bandwidth d-SNOB pulses (352 μT peak B_1 strength, no interpulse delay). The error bars represent the mean ± the standard deviation ($n = 4$). The dashed lines represent exponential decay fits of the signal loss. For a given saturation time, the CEST contrast decreased roughly logarithmically with decreasing M13–based biosensor concentration (a, b, c, inset).

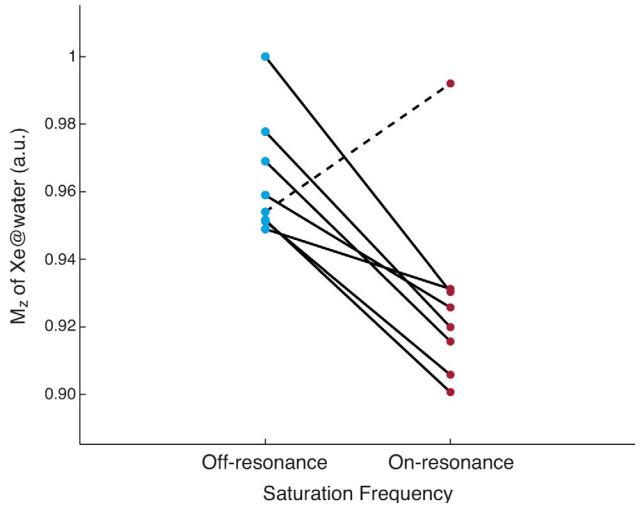

FIG. 7. Detection of a 230 fM sample of the M13-based biosensor. Shown is the residual Xe@water signal following a 20 s saturation train of 3 kHz bandwidth d-DSNOB pulses applied at the ^{129}Xe@CryA frequency (on-resonance) and at an equal distance on the downfield side of the ^{129}Xe@water frequency (off-resonance). An outlying on-resonance data point is shown by the dashed line. Both groupwise and paired Student's *t*-tests showed significant contrast (4.8%, or 3.7% with inclusion of the outlier) between the data sets corresponding to the two saturation frequencies ($P < 0.01$). [Color figure can be viewed in the online issue, which is available at wileyonlinelibrary.com.]

previous reports using continuous wave-based saturations (13) highlights the utility of using d-SNOB trains with higher B_1 strengths for saturating exchanging solvated xenon signals (37). Modest decreases in the per-CryA sensitivity were observed with respect to a similar hyperCEST study using d-SNOB based saturation (27), which may be due to enhanced xenon binding or exchange dynamics associated with the viral capsids used in that study, or due to possible differences in the experimental conditions—namely the ^{129}Xe polarization level. We hypothesize that the sensitivity gain may arise from semicoherent inversions of the slowly exchanging xenon spins [$\tau_{Xe@CryA}$ is approximately 6 ms at 310 K (38)] when using short strong d-SNOB pulses, thus increasing the dynamic range of the altered M_z being passed back to the bulk Xe@water pool. Another possible mechanism for the increased per-CryA sensitivity may be solubility-driven conformational changes to CryA when bound to the phage that enhance their accessibility for xenon binding (39), although this explanation would need to be rectified with the similar hyperCEST responses observed for the unscaffolded and phage-bound versions of CryA.

When considering SAR constraints for in vivo applications of ^{129}Xe-based biosensors, it is favorable to note that due to the low gyromagnetic ratio of ^{129}Xe relative to ^{1}H, the peak B_1 field strengths reported must be divided by 3.62 when comparing to SAR equivalents of saturations applied at ^{1}H carrier frequencies for experiments such as PARACEST and magnetization transfer (i.e., SAR $\propto w_1^2, w_0^2$). Furthermore, some preliminary results suggest that lower duty cycle d-SNOB saturation trains using interpulse delays may allow for much lower SAR envelopes while realizing only modest reductions in CEST contrast (37).

The dramatic sensitivity demonstrated by the M13-based ^{129}Xe biosensors make them an advantageous choice for further development toward targeted molecular MRI applications. Continuing work will be focused on investigating the utility and biocompatibility of antibody-targeted versions of the M13-based biosensor for cellular recognition applications.

ACKNOWLEDGMENTS

The authors would like to thank the laboratory of James D. Marks at the University of California San Francisco for providing the unmodified M13 bacteriophage. The development and execution of ^{129}Xe NMR techniques was supported by NSERC (T.K.S.) and the U.S. Department of Energy. The development of chemical modification techniques for filamentous phage was supported by the U.S. Department of Defense Breast Cancer Research Program. The authors T.K.S. and K.K.P. contributed equally to this work.

APPENDIX A—CHEMICAL SYNTHESIS AND CHARACTERIZATION

General Synthesis

All chemical reagents were of analytical grade, obtained from commercial suppliers, and used without further purification unless otherwise noted. Organic extracts were dried over $MgSO_4$ and solvents were removed with a rotary evaporator at reduced pressure. Flash chromatography was performed using Silicycle Siliaflash P60 40–63 Å 230–400 mesh silica gel. NMR spectra were acquired using a Bruker AV-600, AV-500, AVQ-400, or AVB-400 spectrometer.

RP-HPLC

Peptide constructs were purified by RP-HPLC using a Rainin Instruments Dynamax SD-200 system equipped with a Varian UV-Vis detector (model 345) and a Microsorb C18 analytical column (4.6 × 250 mm) at a flow rate of 1 mL/min, a semipreparative column (10 × 250 mm) at a flow rate of 4 mL/min, or a preparative column (21.4 × 250 mm) at a flow rate of 20 mL/min. A binary solvent system consisting of buffer A [0.1% trifluoroacetic acid in water (v/v)] and buffer B [0.1% trifluoroacetic acid in acetonitrile (v/v)] was used. HPLC samples were filtered through a 0.2 μm membrane prior to injection.

RP-HPLC of bacteriophage M13 was performed on an Agilent 1100 Series HPLC System (Agilent Technologies). Sample analysis for all HPLC experiments was achieved with an inline diode array detector. An Agilent Zorbax 300 SB-CN column was used for all measurements. A binary solvent system consisting of buffer A [0.1% trifluoroacetic acid in water (v/v)] and buffer B [0.1% trifluoroacetic acid in acetonitrile (v/v)] was used. The elution gradient was 35% buffer B for the first 4 min, ramping to 70% buffer B over 15 min, then to 95% buffer B over the next 30 s, and a 10 min wash with 95%. Typical p8 elution time was 10–13 min.

N′-Boc-aminoxyacetyl-*N*-hydroxysuccinimide Ester (1)

To a stirred solution of *N*-Boc-aminooxyacetic acid (500 mg, 2.62 mmol) in dichloromethane (30 mL) cooled on an ice bath were added *N*-hydroxysuccinimide (332 mg, 2.88 mmol) and *N,N′*-dicyclohexylcarbodiimide (594 mg, 2.88 mmol). The solution was stirred for 5 min after which it was removed from the ice bath and stirred at room temperature for 45 min. The reaction was quenched with addition of dichloromethane, filtered through a pad of Celite, and the filtrate was washed with sat. $NaHCO_3$ (2 × 40 mL). The organic phase was dried over $MgSO_4$ and concentrated under vacuum. The white solid was used as is. ^1H NMR (400 MHz, $CDCl_3$): δ = 7.67 (1H, s), 4.78 (2H, s), 2.88 (4H, s), 1.49 (9H, s). ^{13}C NMR (151 MHz, $CDCl_3$): δ = 168.8, 165.2, 156.4, 82.8, 71.0, 28.3, 25.8. ESI-HRMS calcd for $C_{11}H_{16}N_2O_7$ [M + Na]: 311.0858 Da, found 311.0852 Da [M + Na].

Fmoc-Lys[Boc-aminooxyacetyl]—OH (2)

To a stirred solution of the ester **1** (700 mg, 2.43 mmol) and the TFA salt of Fmoc-Lysine (1.24 g, 2.67 mmol) in dry methylene chloride (30 mL) was added *N,N*-diisopropylethylamine (1.59 mL, 9.17 mmol). The solution was stirred at room temperature for 11 h. The reaction was quenched with addition of dichloromethane and washed with sat. NH_4Cl (1 × 40 mL). The aqueous phase was extracted with dichloromethane (3 × 20 mL), then the organic phases were combined, dried over $MgSO_4$, and concentrated under vacuum. Purification by silica gel chromatography using 1:4 ethyl acetate:hexanes with 1% acetic acid gave the desired aminooxy functionalized amino acid as an off-white residue. Resolving the residue in dichloromethane and adding it dropwise to a solution of hexanes precipitated the product as a white solid (757 mg, 58%). ^1H NMR (600 MHz, $CDCl_3$): δ = 8.27 (1H, broad s), 7.75 (2H, d, J = 7.8 Hz), 7.60 (2H, dd, J = 7.2 Hz, 11.4 Hz), 7.38 (2H, t, J = 7.2 Hz), 7.29 (2H, t, J = 7.2 Hz), 5.82 (1H, s), 4.46–4.32 (2H, m), 4.29 (2H, s), 4.18 (1H, t, J = 7.2 Hz), 3.40–3.29 (2H, m), 1.93–1.75 (2H, m), 1.63–1.54 (2H, m), 1.44, (9H, s), 1.41–1.27 (2H, m). ^{13}C NMR (151 MHz, $CDCl_3$): δ = 174.9, 169.9, 158.2, 156.5, 144.0, 141.5, 127.9, 127.3, 125.4, 120.2, 83.5, 76.1, 67.2, 54.0, 47.4, 38.6, 31.7, 28.8, 28.3, 22.2. ESI-HRMS(+) calcd for $C_{28}H_{36}N_3O_8$ $[M+H+Na]^+$: 564.2324 Da, found 564.2307 Da $[M+H+Na]^+$.

Aminooxy-Functionalized CryA-Peptide (CryA—ONH_2)

The aminooxy-functionalized CryA-peptide was synthesized in four parts. First, a water solubilizing tetraglutamic acid peptide, Glu–Glu–Glu–Glu (EEEE-resin), was prepared on Wang resin (1.2 mmol/g, 100–200 mesh) using standard Fmoc solid-phase peptide synthesis with N_α-Fmoc protected amino acids, *N,N*-diisopropylethylamine, and 1-hydroxybenzotriazole (HOBT)/*O*-(benzotriazol-1-yl)-*N,N,N′,N′*-tetramethyluronium hexafluorophosphate (HBTU) ester activation in *N,N*-dimethylformamide. A 5-fold excess of amino acid was used for the coupling steps, which involved gentle rotation for 3 h. Fmoc removal was achieved with 20% piperidine in *N,N*-dimethylformamide (2 × 10 min). Next, the aminooxy functionality was installed by coupling **2** following the same solid-phase peptide synthesis conditions above, except that the coupling was allowed to proceed with gentle rotation for 5 h. Subsequently, a linker was installed using Fmoc-6-aminohexanoic acid and the same solid-phase peptide synthesis conditions as above. Finally, the peptide was capped at the N-terminus using a 2.5-fold excess of the Cryptophane-A monoacid cage (monoacid CryA supplied by Kang Zhao, Tianjin University, China) using the same solid-phase peptide synthesis conditions as above, except that the coupling was allowed to proceed with gentle rotation for 12 h. The product was cleaved using a cocktail of trifluoroacetic acid:water:triisopropylsilane (95:2.5:2.5) for 2.5 h and then precipitated in methyl *tert*-butyl ether. The crude product was purified by RP-HPLC using a C18 column with a gradient from 40 to 60% buffer B over 30 min. A 8 mM stock solution of the aminooxy-functionalized CryA-peptide construct was prepared by dissolving the purified solid in Dulbecco's phosphate-buffered saline and adjusting the pH with sodium hydroxide until the solution became clear. ESI-MS(–) calcd for $C_{89}H_{108}N_8O_{30}$ $(M–3H)^{3–}$: 588.57 Da found 588.49 Da $(M–3H)^{3–}$.

REFERENCES

1. Caravan P, Ellison JJ, McMurry TJ, Lauffer RB. Gadolinium(III) chelates as MRI contrast agents: structure, dynamics, and applications. Chem Rev 1999;99:2293–2352.
2. Woods M, Woessner DE, Sherry AD. Paramagnetic lanthanide complexes as PARACEST agents for medical imaging. Chem Soc Rev 2006;35:500–511.
3. Bulte JWM, Kraitchman DL. Iron oxide MR contrast agents for molecular and cellular imaging. NMR Biomed 2004;17:484–499.
4. Chen J, Lanza GM, Wickline SA. Quantitative magnetic resonance fluorine imaging: today and tomorrow. Wiley Interdiscip Rev Nanomed Nanobiotechnol 2010;2:431–440.
5. Kurhanewicz J, Bok R, Nelson SJ, Vigneron DB. Current and potential applications of clinical 13C MR spectroscopy. J Nucl Med 2008; 49:341–344.
6. Guenther D, Hanisch G, Kauczor HU. Functional MR imaging of pulmonary ventilation using hyperpolarized noble gases. Acta Radiol 2000;41:519–528.
7. Oros A-M, Shah NJ. Hyperpolarized xenon in NMR and MRI. Phys Med Biol 2004;49:R105–R153.
8. Ardenkjær-Larsen JH, Fridlund B, Gram A, Hansson G, Hansson L, Lerche MH, Servin R, Thaning M, Golman K. Increase in signal-to-noise ratio of > 10,000 times in liquid-state NMR. PNAS 2003;100: 10158–10163.
9. Kuhn LT, Bommerich U, Bargon J. Transfer of parahydrogen-induced hyperpolarization to 19F. J Phys Chem A 2006;110:3521–3526.
10. Dobrucki LW, Sinusas AJ. PET and SPECT in cardiovascular molecular imaging. Nat Rev Cardiol 2010;7:38–47.
11. Spence MM, Rubin SM, Dimitrov IE, Ruiz EJ, Wemmer DE, Pines A, Yao SQ, Tian F, Schultz PG. Functionalized xenon as a biosensor. Proc Natl Acad Sci USA 2001;98:10654–10657.
12. Schröder L, Lowery TJ, Hilty C, Wemmer DE, Pines A. Molecular imaging using a targeted magnetic resonance hyperpolarized biosensor. Science 2006;314:446–449.
13. Schröder L, Meldrum T, Smith M, Lowery TJ, Wemmer DE, Pines A. Temperature response of (129)Xe depolarization transfer and its application for ultrasensitive NMR detection. Phys Rev Lett 2008; 100:257603–257606.
14. Gabard J, Collet A. Synthesis of a (D3)-bis(cyclotriveratrylenyl) macrocage by stereospecific replication of a (C3)-subunit. J Chem Soc, Chem Commun 1981;21:1137–1139.
15. Spence MM, Ruiz EJ, Rubin SM, Lowery TJ, Winssinger N, Schultz PG, Wemmer DE, Pines A. Development of a functionalized xenon biosensor. J Am Chem Soc 2004;126:15287–15294.
16. Wei Q, Seward GK, Hill PA, Patton B, Dimitrov IE, Kuzma NN, Dmochowski IJ. Designing 129Xe NMR biosensors for matrix metalloproteinase detection. J Am Chem Soc 2006;128:13274–13283.

17. Roy V, Brotin T, Dutasta J-P, Charles M-H, Delair T, Mallet F, Huber G, Desvaux H, Boulard Y, Berthault P. A cryptophane biosensor for the detection of specific nucleotide targets through xenon NMR spectroscopy. ChemPhysChem 2007;8:2082–2085.
18. Seward GK, Wei Q, Dmochowski IJ. Peptide-mediated cellular uptake of cryptophane. Bioconjug Chem 2008;19:2129–2135.
19. Chambers JM, Hill PA, Aaron JA, Han Z, Christianson DW, Kuzma NN, Dmochowski IJ. Cryptophane xenon-129 nuclear magnetic resonance biosensors targeting human carbonic anhydrase. J Am Chem Soc 2009;131:563–569.
20. Schlundt A, Kilian W, Beyermann M, Sticht J, Günther S, Höpner S, Falk K, Roetzschke O, Mitschang L, Freund C. A xenon-129 biosensor for monitoring MHC-peptide interactions. Angew Chem Int Ed Engl 2009;48:4142–4145.
21. Boutin C, Stopin A, Lenda F, Brotin T, Dutasta J-P, Jamin N, Sanson A, Boulard Y, Leteurtre F, Huber G, Bogaert-Buchmann A, Tassali N, Desvaux H, Carrière M, Berthault P. Cell uptake of a biosensor detected by hyperpolarized 129Xe NMR: the transferrin case. Bioorg Med Chem 2011;19:4135–4143.
22. Chen RY, Fan FC, Kim S, Jan KM, Usami S, Chien S. Tissue-blood partition coefficient for xenon: temperature and hematocrit dependence. J Appl Physiol 1980;49:178–183.
23. Wolber J, Cherubini A, Dzik-Jurasz AS, Leach MO, Bifone A. Spin-lattice relaxation of laser-polarized xenon in human blood. Proc Natl Acad Sci USA 1999;96:3664–3669.
24. Albert MS, Balamore D, Sakai K, Kacher D, Walsworth RL, Oteiza E, Jolesz FA. Hyperpolarized 129Xe Lifetimes in Blood. In: Proceedings of the 4th Annual Meeting of ISMRM, New York, New York, USA, 1996. p. 1357.
25. Venkatesh AK, Zhao L, Balamore D, Jolesz FA, Albert MS. Evaluation of carrier agents for hyperpolarized xenon MRI. NMR Biomed 2000;13:245–252.
26. Mynar JL, Lowery TJ, Wemmer DE, Pines A, Fréchet JMJ. Xenon biosensor amplification via dendrimer-cage supramolecular constructs. J Am Chem Soc 2006;128:6334–6335.
27. Meldrum T, Seim KL, Bajaj VS, Palaniappan KK, Wu W, Francis MB, Wemmer DE, Pines A. A xenon-based molecular sensor assembled on an MS2 viral capsid scaffold. J Am Chem Soc 2010;132:5936–5937.
28. Vasalatiy O, Gerard RD, Zhao P, Sun X, Sherry AD. Labeling of adenovirus particles with PARACEST agents. Bioconjug Chem 2008;19:598–606.
29. Marks C, Marks JD. Phage libraries—a new route to clinically useful antibodies. N Engl J Med 1996;335:730–733.
30. Liu B, Conrad F, Cooperberg MR, Kirpotin DB, Marks JD. Mapping tumor epitope space by direct selection of single-chain Fv antibody libraries on prostate cancer cells. Cancer Res 2004;64:704–710.
31. Li K, Chen Y, Li S, Nguyen HG, Niu Z, You S, Mello CM, Lu X, Wang Q. Chemical modification of M13 bacteriophage and its application in cancer cell imaging. Bioconjug Chem 2010;21:1369–1377.
32. Witus LS, Francis MB. Using synthetically modified proteins to make new materials. Acc Chem Res 2011;44:774–783.
33. Stephanopoulos N, Francis MB. Choosing an effective protein bioconjugation strategy. Nat Chem Biol 2011;7:876–884.
34. Gilmore JM, Scheck RA, Esser-Kahn AP, Joshi NS, Francis MB. N-terminal protein modification through a biomimetic transamination reaction. Angew Chem Int Ed Engl 2006;45:5307–5311.
35. Schlick TL, Ding Z, Kovacs EW, Francis MB. Dual-surface modification of the tobacco mosaic virus. J Am Chem Soc 2005;127:3718–3723.
36. Kupce E, Boyd J, Campbell ID. Short selective pulses for biochemical applications. J Magn Reson B 1995;106:300–303.
37. Meldrum T, Bajaj VS, Wemmer DE, Pines A. Band-selective chemical exchange saturation transfer imaging with hyperpolarized xenon-based molecular sensors. J Magn Reson 2011;213:14–21.
38. Chavez LJ, PhD thesis, Chemistry (supervisor: Alex Pines), University of California Berkeley, 2007, 69 p.
39. Taratula O, Hill PA, Khan NS, Carroll PJ, Dmochowski IJ. Crystallographic observation of “induced fit” in a cryptophane host-guest model system. Nat Commun 2010;1:148.